Journal of Materials Research and Technology 30 (2024) 3571–3583

Contents lists available at ScienceDirect

Journal of Materials Research and Technology

journal homepage: www.elsevier.com/locate/jmrt

Development of a gas metal arc based prototype for direct energy deposition with micrometric wire

Paulo Henrique Grossi Dornelas [a,*], J.P. Oliveira [a,b], Tadeu Castro da Silva [c,d], A.S. Ramos [e], Telmo G. Santos [a,f]

[a] UNIDEMI, Department of Mechanical and Industrial Engineering, NOVA School of Science and Technology, Universidade NOVA de Lisboa, 2829-516, Caparica, Portugal
[b] CENIMAT/I3N, Department of Materials Science, NOVA School of Science and Technology, Universidade NOVA de Lisboa, 2829-516, Caparica, Portugal
[c] Additive Manufacturing and Tooling Group, Federal University of Technology – Paraná, R. Deputado Heitor Alencar Furtado, 5000, Curitiba, PR, 81280-340, Brazil
[d] LOM, Department of Mechanical Engineering, Fluminense Federal University, Niteroi RJ, 24210-240, Rio de Janeiro, Brazil
[e] CEMMPRE, Department of Mechanical Engineering, University of Coimbra, R. Luís Reis Santos, Coimbra, 3030-788, Portugal
[f] Laboratório Associado de Sistemas Inteligentes, LASI, 4800-058, Guimarães, Portugal

ARTICLE INFO

Handling editor: L Murr

Keywords:
Micro additive manufacturing
Direct energy deposition
Process downscaling

ABSTRACT

In recent years, efforts have been focused on the development of metal additive manufacturing (AM) processes to address the growing trend of miniaturization in industries such as aerospace and electronics. Thus, new technologies have been developed based on a downscaled approach using direct energy deposition (DED) processes, now referred to as μ-DED. In this context, the development of a downscaled DED prototype based on gas metal arc (GMA) working with micrometric wires (μ-GMA) has the potential to unify the positive characteristics of GMA-based DED, increasing the complexity of the design and resolution of the produced parts. Therefore, this work focuses on developing a μ-GMA prototype and assessing its technical feasibility. This paper describes the development of the μ-GMA prototype, characterizes the metallic transfer mode, and statistically analyzes the effect of deposition parameters on bead width and height. Additionally, microstructural analysis, Vickers microhardness, and reduced Young's modulus tests were performed. The μ-GMA prototype demonstrated the capability to deposit beads with an approximate width of 1 mm, nearly 5 times thinner than standard GMA-based DED deposition, with a build rate of 30 cm^3/h, which is lower than GMA-based DED but higher than other μ-DED processes. Furthermore, the mechanical properties of the μ-GMA depositions are comparable to regular GMA-based DED parts.

1. Introduction

Additive manufacturing (AM) is an emerging technology due to its ability to fabricate parts on demand with geometric freedom and the possibility for mass customization [1], low cost-effectiveness for small batch manufacturing [2], and is highlighted as one of the pillars of Industry 4.0 due to its high level of automation and customization potential [3]. AM allows fast prototyping and part optimization [4], making it a promising technology compared to milling and molding, especially when the complexity of design and customization is needed [5]. In addition, AM is an environmentally friendly manufacturing technology, diminishing material waste and promoting energy savings [6].

Among metal AM processes, it is possible to highlight powder-based fusion (PBF) and direct energy deposition (DED) ones due to their industrial scalability and technological maturation. PBF processes [7] are characterized by the spreading and selective melting/sintering of successive thin beads of metallic powder using a high-power laser or electron beam to produce dense parts with good mechanical properties. This process occurs in a controlled atmosphere (i.e., a sealed chamber), in which shielding gas is fed to protect the melt pool and prevent powder oxidation. Due to the focused beam heat source, these processes have high accuracy, allowing complexity in design and the possibility of printing reactive materials (in a shielded atmosphere). However, health and environmental risks related to metallic powder handling, low build rates, limitations due to interlayer support, and high acquisition costs of

* Corresponding author.
E-mail address: p.dornelas@campus.fct.unl.pt (P.H.G. Dornelas).

https://doi.org/10.1016/j.jmrt.2024.04.056
Received 28 February 2024; Received in revised form 7 April 2024; Accepted 7 April 2024
Available online 16 April 2024

Table 1
Chemical composition (wt.%) of the filler metal.

Material	C	Mn	Si	S	Cr	Ni	Nb + V + Ti	Al	Zn	Fe
Wire	0.09	0.58	0.86	0.11	0.09	0.06	0.05	1.13	0.23	Bal.

raw materials restrict these processes to high-value aggregate parts. On the other hand, DED [8,9] has several variants, which are based on welding processes (e.g., laser, arc plasma, and electron beam) and can use multiple feedstock material types (e.g., metallic powder and wires). Among DED processes, those based on welding techniques such as gas metal arc (GMA), gas tungsten arc (GTA), and plasma transferred arc (PTA) are classified as wire and arc additive manufacturing (WAAM). Each variant is more suitable for specific applications, such as cost-acquisition, heat input (H), dimensional accuracy, and build rate [10]. In recent years, DED processes have been developed to provide solutions for ever-increasing miniaturization requirements, with studies focusing on increasing process resolution, now referred to as μ-DED [11].

The μ-DED processes are still pioneering technologies and have been underexplored in the literature, making them a promising field of study. The μ-DED technologies have been developed following the downscaling approach, i.e., working with a smaller heat source and thinner filler metal. A summary of the μ-DED techniques available in the literature is described as follows. Three-dimensional micro-welding (3DMW) [12] is a GTA-based DED method conceived to manufacture micro-scale metal components utilizing micrometric metal wire and a pulsed micro-arc. The methodology of 3DMW involves the successive deposition of molten metal in pin-shaped formations, employing a layer-by-layer strategy following the AM approach. The typical 3DMW system is composed of a welding station, an arc control unit, system control computers, a video-monitoring device, heating and water-cooling systems coupled with the substrate, as well as two opposed wire-feeders, which allow the deposition of components with graded compositions and intermetallic alloys. This prototype used wire of Ø 200 μm and successfully deposited pure metals (Ti), intermetallics (Ni–Al, Ti–Ni, Ti–Fe), alloys (Inconel 600, SS304, and Invar 42), and compositionally graded materials (FMG) [12–16]. The technology exhibits promise owing to the low heat input characteristic inherent to the GTA process and the capability to work with millimetric wires. This prototype potentially enables the production of parts characterized by high resolution and favorable mechanical properties, attributed to reduced internal stress. However, the extremely low deposition rate of this prototype limits its practical applications to research settings. Micro-plasma transferred arc (μ-PTA) [17] is a variant of the PTA technique, specifically tailored for repairing defective dies and molds, as well as constructing meso-size, high-value components through small layer deposition. In the literature, advancements in μ-PTA have been documented under two main approaches: micro-plasma wire deposition (μ-PTAWD) [17,18], utilizing Ø 300 μm wire as filler metal, and metallic powder-based deposition (μ-PTAPD) [19–21], suitable for hard and brittle alloys, functionally graded materials (FMG), and refractory alloys. The μ-PTAWD prototype integrates a plasma welding system, including a micro-plasma torch, a custom-built power supply, a modified nozzle, and a wire feed system calibrated for thinner wires to feed into the melt pool, alongside a moving XY worktable. μ-PTAWD depositions achieved bead thicknesses smaller than 2000 μm, operating within a build rate range of 5–50 cm^3/h [17]. Reported deposition defects include discontinuities in layers due to over-melting and filler metal evaporation, as well as inadequate melting and bonding between layers resulting from unsuitable process parameters such as plasma power and wire feed rate. Although efforts have been directed towards enhancing μ-PTAWD systems to deposit smooth layers with high accuracy, there remains a lack of results concerning the printing of other metals and their corresponding mechanical properties. Several studies have concentrated on advancing μ-laser melting deposition (μ-LMD) systems, employing a scaled-down approach from traditional LMD setups [22–27]. These prototypes utilize micrometric laser spot sizes, micrometric wire for filler metal, and a 3-axis moving table. μ-LMD systems stand out as the most promising μ-DED technology, capable of depositing thin layers (166 μm) and flawlessly constructing walls with an aspect ratio of up to 20. They operate with wires as small as ø = 0.1 mm and a variety of raw materials. Notably, the superior dimensional accuracy observed in the deposited parts stems from the utilization of a high-energy laser as the heat source, distinguishing it from other μ-DED technologies reliant on electric arcs. In addition, the present authors performed a comprehensive review article [11] showcasing a state-of-the-art analysis of the existing body of knowledge on this topic, including the existing μ-DED technologies. This comparison goes beyond the process and deposited bead features to encompass aspects such as cost-related factors, health risks, and environmental considerations. We reported the development of new systems based on a downscaling approach, which successfully achieved an increase in resolution and surface finishing.

GMA-based DED processes possess high build rates, making them attractive for industrial settings. Additionally, they have lower system and raw material acquisition costs, generate fewer deposition fumes, and consequently pose fewer risks to workers' health and the environment. However, GMA-based DED is inherently limited to building small components with smooth and detailed features due to the larger wire diameter used (Ø ~ 1.0 mm) compounded by the large heat source dimensions, often resulting in deposited beads with widths above 5 mm [28]. Therefore, the development of a downscaled GMA-based prototype, e.g., working with micrometric wires, has the potential to combine the favorable characteristics of GMA and increase the complexity of the design and resolution of the parts produced. However, in contrast to the cited μ-DED technologies, GMA does not utilize an external heat source; the electric arc is established between the filler metal and the substrate, making these downscaling dynamics complex. In other words, will the metallic transfer dynamics be the same, once the applied current must be smaller due to the thinner wire? How much do the lower currents affect the cooling rate? Does the relationship between deposition parameters and bead dimensions occur similarly to regular GMA-based AM? What will be the resultant microstructure and mechanical properties?

Driven by the challenges previously described and the potential to combine the favorable characteristics of GMA, thus enhancing its resolution capability for the μ-DED context, this pioneering work proposes to develop a micro gas metal arc (μ-GMA) DED prototype (a downscaled GMA approach for the deposition of a Ø 300 μm low-carbon steel wire) and to assess its technical feasibility. This work describes the development of the μ-GMA prototype, characterizes the metallic transfer mode, analyzes the effect of deposition parameters such as wire feeding (WFS) and travel speed (TS) on bead width (BW) and height (BH). Microstructural analysis was performed using scanning electron microscopy, mechanical properties were measured using Vickers microhardness, and the reduced Young's modulus was determined from nanoindentation mapping. Additionally, this work compares μ-GMA with a standard GMA-based DED process, contrasting their fundamental differences.

2. Experimental procedure

2.1. Materials

A Ø 300 μm low-carbon steel wire was used in this work. For μ-GMA single and multi-bead wall deposition, a hot-rolled 50 × 120 × 0.6 mm low-carbon steel plate served as the substrate. Before deposition, the

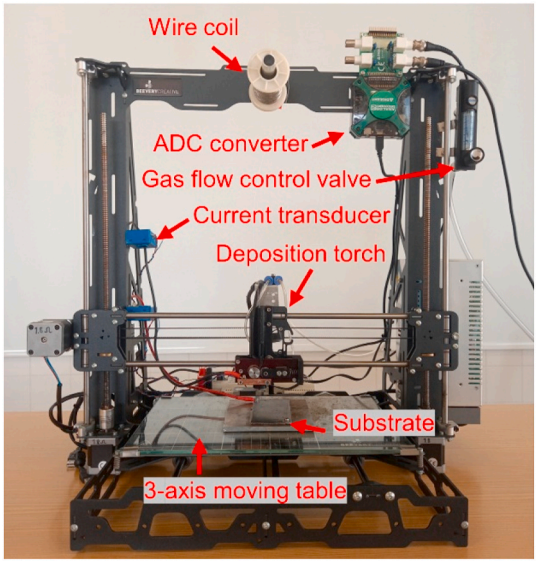

Fig. 1. General view of the μ-GMA prototype.

substrate was sanded, polished, and cleaned to prevent impurities and oxidation, ensuring repeatable and steady-state deposition conditions. The filler metal chemical composition was obtained from optical emission spectroscopy and is available in Table 1.

2.2. Experimental setup

Feeding wires with Ø ≤ 300 μm presents a significant challenge because modern GMA-based 3D printers typically have a lower limit for wire diameters of 0.7–0.8 mm. These printers are typically composed of a commercial welding power source, a control unit, an automatic wire feeder, a torch, and a robotic arm (or a 3-axis positional system). Therefore, an in-house customized 3D printer was designed, developed, and produced to accommodate wires with Ø ≤ 300 μm. Fig. 1 illustrates the developed μ-GMA prototype.

2.2.1. Torch development

One of the functionalities of a deposition torch in a GMA-based DED process is to establish and maintain electrical contact with the electrode while directing it toward the molten pool. Thus, a specialized nozzle was designed utilizing a C18150 Cu-based alloy, with an external diameter of 6 mm and a wire hole diameter of 0.33 mm. This custom-designed nozzle was threaded into a solid copper straight parallelepiped featuring a 6 mm circular aperture, as depicted in Fig. 2a. Additionally, this prototype features a bi-polar stepper motor coupled with a pulley pressed against a bearing, serving as a wire feed mechanism that continuously feeds the wire toward the melting pool. These systems are attached to a polymer-made plate for electrical isolation from the nozzle. The torch chassis was manufactured using polylactic acid (PLA) through the material extrusion 3D printing process. A 3-axis moving table was adapted from a commercial 3D printer, specifically the B2X300 Creality 3D® model. Control of the 3-axis moving table and wire feeding was achieved using Repetier Software® and an Arduino Mega 2560 microcontroller board.

Aiming to supply shielding gas to protect the molten pool from oxidation, a customized gas feeder was also developed. In this approach, the shielding gas is supplied through two hoses inserted into respective holes located on the backside, as shown in Fig. 2a. The gas then travels through a straight cylindrical to a circular cylindrical channel (ring shape), which features 6 gas ejection apertures around the wire. These apertures are evenly positioned at 60° intervals, with the electrode axis

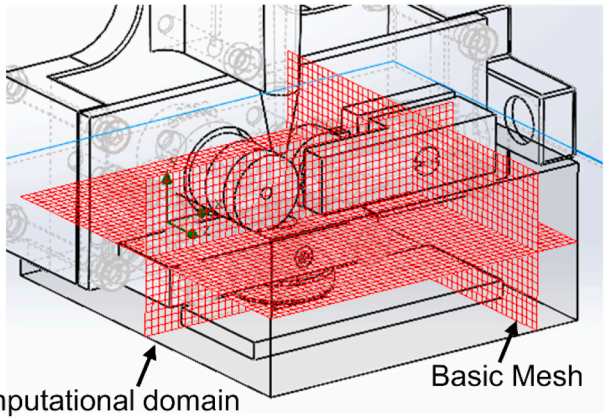

Fig. 3. View of Solidworks Flow Simulation® showing the computational domain and basic mesh.

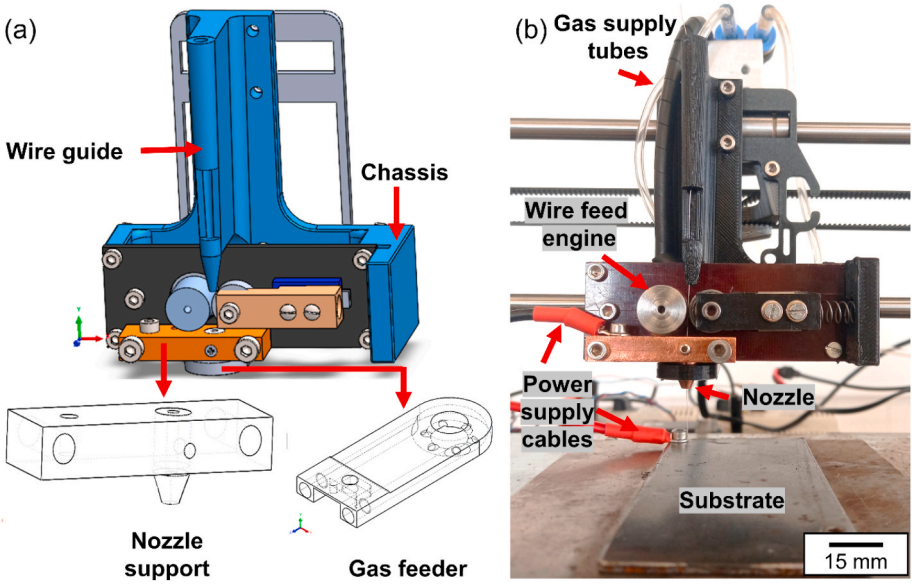

Fig. 2. (a) Computer-aided design of the torch (b) the customized μ-GMA torch.

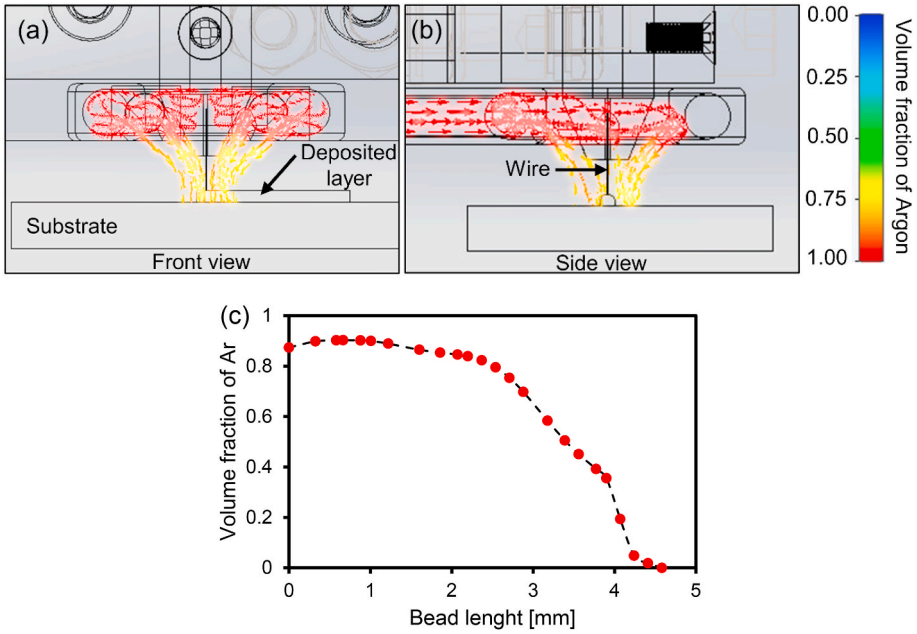

Fig. 4. Illustrative (a) front, and (b) side views of the simulation results for gas flow performed in the gas feeder, and (c) volume fraction of argon according to the bead length.

Table 2
Process parameters of μ-GMA depositions.

Process parameters	Unit	μ-GMA
Voltage $_{NO\ LOAD}$	[V]	17.5
Current $_{MAX}$	[A]	60
Polarity	[−]	DCEP
CTWD	[mm]	5
Shielding gas rate	[l/min]	10
Travel speed	[mm/s]	3–8
Wire feeding speed	[mm/s]	30–150

serving as the center of rotation. The gas feeder model was designed in Solidworks® software. The sizing and angle of the gas-blowing openings were optimized using Computational Fluid Dynamics (CFD) in the Flow Simulation® studio to protect the molten pool from oxidation. The contact-tip-to-work distance (CTWD) used was 5 mm. These simulations were performed based on the well-known Navier-Stokes equations (I and II) for an incompressible fluid in a laminar regime, i.e., the gradient of the flow velocity (u) is zero to satisfy the mass conservation principle (equation I), and the fundamental conservation of momentum (equation II) describes the behavior of fluid flow, where ρ,u,t,P, and ν represent the density, velocity vector, time, pressure, and kinematic viscosity of the fluid, respectively. The simulations were performed considering the following boundary conditions at 20 °C: 10 L/min inlet flow (u) of pure argon gas (5 L/min inlet flow in each opening), output pressure (P) of 1.03×10^5 Pa (atmospheric pressure), and the outside environment is initially composed by 100% air. The computational domain was 66 × 30 × 74 mm with a mesh size of 2 mm, as illustrated in Fig. 3. The final design was confirmed when an atmosphere with an argon volume exceeding 80% was guaranteed at a 2 mm distance from the point of contact between the wire and the weld pool. Fig. 4a and b illustrate the gas flow path from the gas feeder to the substrate, while Fig. 4c shows that the gas feeder ensures good shielding (above 80% argon) until 2.5 mm of the wire contact point in the substrate. The optimized gas feeder was 3D printed using PLA as the raw material.

$$\nabla \bullet u = 0 \tag{1}$$

$$\frac{\partial u}{\partial t} + (\nabla \bullet u) \bullet u = -\frac{1}{\rho} \bullet \nabla P + \nu \bullet \nabla^2 u \tag{2}$$

2.2.2. Power supply

The electric power conditions for such reduced wires (Ø ≤ 300 μm) are also a challenge, as conventional commercial welding power sources are typically oriented for much higher power intensity. To provide suitable I–V characteristics for small welding energy, a Keithley 720W (constant voltage mode) was used as the power supply, in parallel with a 160,000 μF electrolytic capacitor. Electric resistances in series with the positive electrode (DCEP) were employed to limit the welding current to 60 A (preliminary tests indicated that higher current values caused instabilities in the transfer mode due to the high power relative to the low diameter wire). Voltage and current curves were measured using a current transducer LEM HTA 600-S and a 14-bit ADC converter Digilent Analog Discovery 2 operating at 800 K samples/sec.

2.3. Preliminary tests of deposition parameters

According to the literature, functional GMA-based DED working parameters for Ø 0.8–1 mm wire are in the range of voltage 16–24 V and WFS of 3–15 m/min [28–30]. However, the deposition parameters for a 300 μm wire will be different. To comprehend and establish the μ-GMA process parameters, a series of exploratory tests were performed, varying voltage, upper current limit, CTWD, shielding gas rate, TS, and WFS. From these preliminary results, the values of voltage setup (17.5 V), maximum current (60 A), CTWD (5 mm), and shielding gas rate (99% Ar at 10 L/min) were selected and kept constant to determine the operational working window in terms of TS and WFS. Table 2 details the process parameters adopted during μ-GMA depositions. A map was constructed using different combinations of TS and WFS (Fig. 5), and the deposited beads were classified as continuous, discontinuous, or overfed (BW ≥ 2 mm). Each μ-GMA deposition was performed in duplicate and in a randomized order. The deposition parameters WFS = 120 and TS = 5 mm/s were selected, and an 8-bead wall was built to demonstrate the feasibility of the μ-GMA technique (Fig. 6).

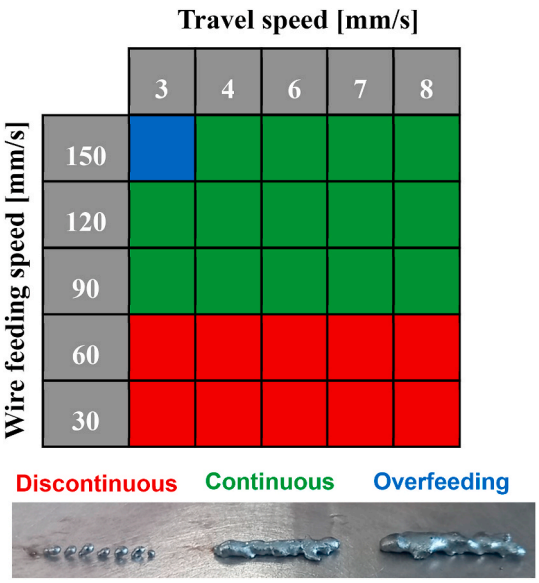

Fig. 5. (a) Wire feeding and travel speed (mm/s) map indicating discontinuous, continuous, and overfeeding characteristics.

Table 3
Deposition parameters of the design of experiments.

Design parameter	Unit	Low (−1)	Central point (0)	High (1)
Travel speed	[mm/s]	4	6	8
Wire feeding speed	[mm/s]	90	120	150
Constant parameters	**Unit**	**Values**		
Voltage $_{NO\ LOAD}$	[V]	17.5		
Current $_{MAX}$	[A]	60		
CTWD	[mm]	5		
Stick-out	[mm]	1		
Shielding gas rate	[L/min]	10		

Table 4
Bead height (BH) and width (BW) models summary showing goodness of fit metrics.

Regression statistic	BW	BH
R^2	0.973	0.934
R^2_{adj}	0.968	0.925
R^2_{pred}	0.951	0.907

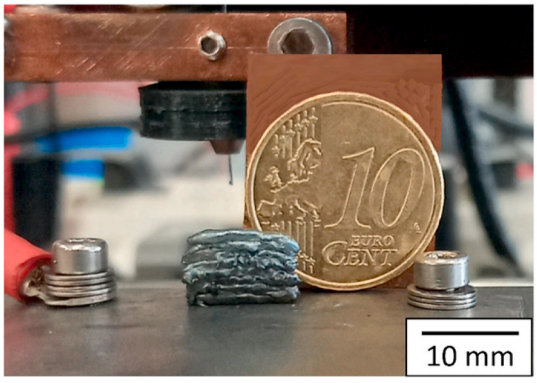

Fig. 6. 8-bead wall deposition performed by μ-GMA showing the prototype feasibility. This deposition was performed using WFS = 120 mm/s, and TS = 5 mm/s.

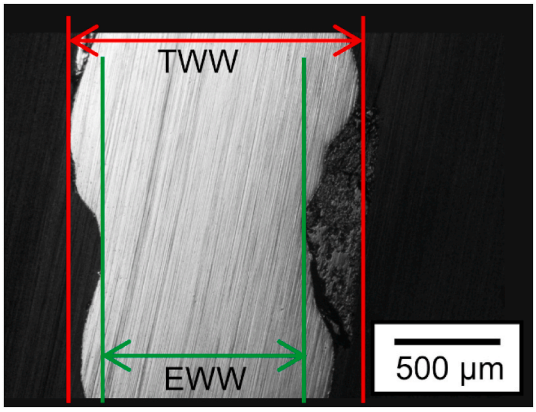

Fig. 7. Cross-sectional micrograph illustrating an example of a measure of the effective wall width (EWW) and total wall width (TWW) from a μ-GMA deposition.

2.4. Sample building strategies

In the first stage of μ-GMA experiments, 10-mm-long single beads were deposited away from each other by 5 mm on the x-axis and 10 mm on the y-axis. The successive overlapped beads were deposited continuously, i.e., without a delay time between the layers. To keep the CTWD constant, 1 mm was added to the z-axis before initiating the deposition of the superior bead.

2.5. Transfer mode and thermographic characterizations

The metallic transfer mode during deposition was recorded using a high-speed camera, FASTCAM Mini WX, at 4000 fps with a resolution of 1280 × 512 and an 800 nm filter. A Fluke TI400 thermographic infrared camera was employed to acquire the temperature of the beads during the depositions. To ensure accurate temperature measurements, the thermographic infrared camera utilized in this study was calibrated prior to data collection. The camera had an accuracy of ±2%, a measurement limit of 1200 °C, an emissivity of 0.84 [31], a refresh rate of 9 Hz, and a resolution of 320 × 240 pixels. The temperature profile data were compiled using the acquisition software SmartView.

2.6. Dimensional accuracy

The lower dimensional accuracy (DA) characteristic of GMA-based DED leads to higher material wastage after machining. One way to measure this value is to calculate it from the effective wall width (EWW) and total wall width (TWW) according to equation (III) [32]. An 8-bead wall, 10 mm in length, was cross-sectioned at three locations spaced 3 mm apart (i.e., beginning, middle, and end of the wall). DA was calculated as the average of these three measurements. Fig. 7 illustrates the measurement of the EWW (green line) and TWW (red line) of a 2-bead wall deposited by μ-GMA.

$$DA = \frac{TWW - EWW}{2} \quad (3)$$

2.7. Microstructural and microhardness characterizations

Samples for optical and SEM microscopy were cross-sectioned, ground sequentially with 100, 220, 320, 400, 500, 600, and 1200# sandpaper, and then polished sequentially with diamond paste with a particle size of 1 μm. The microstructure was revealed through etching in a solution of 2 mL of nitric acid (HNO_3) in 98 mL of ethyl alcohol (CH_3CH_2OH) for 20 s. Optical microscopy and SEM were performed using a Leica DMI 5000 M and a Quanta 650 FEG, respectively. Microhardness measurements were conducted using a Mitutoyo HM-112

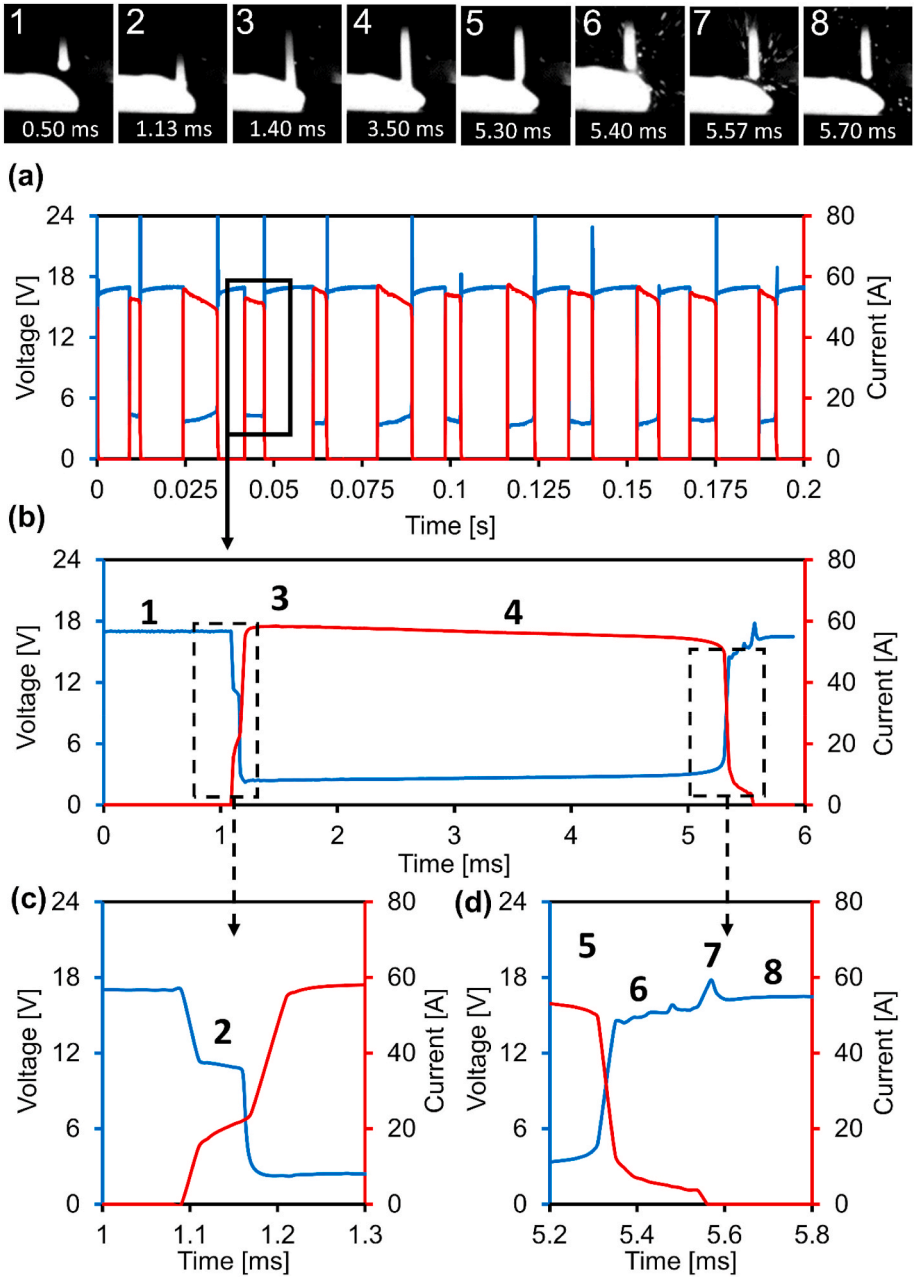

Fig. 8. I–V curves identify the frames of droplet transfer mode from high-speed imaging.

Micro-Vickers Hardness Testing Machine, with a load of 0.1 kg and a dwell time of 10 s, with the distance between indentations set at 100 μm.

2.8. Nanoindentation tests

The mechanical behavior of the low-carbon steel single bead deposited by μ-GMA was evaluated using nanoindentation in a Micro Materials Nano hardness equipment with a Berkovich diamond indenter. The reduced Young's modulus was determined using the Oliver and Pharr analysis method [33]. The nanoindentation experiments were conducted up to a maximum load of 6.2 mN. To obtain the reduced Young's modulus maps from the center of the beads, indentation matrices with 8 rows and 12 columns were defined, resulting in a total of 96 measurements. The distance between rows and columns was set at 15 μm and 10 μm, respectively.

3. Results and discussion

3.1. Metallic transfer mode

The GMA-based DED process has a particular characteristic related to the metallic transfer mode. While laser processes (powder bed fusion and DED), electron beam, GTA, and PTA-based processes utilize an external heat source to melt the filler metal, GMA establishes an electric arc between the molten pool/substrate and the filler metal (electrode). As a result, the electrode melts, and droplets are transferred to the molten pool. However, this droplet transfer phenomenon can occur through different mechanisms (e.g., short-circuit, globular, spray), and it is determined by parameters such as voltage, welding current, shielding gas, wire diameter, and chemical composition [34]. Understanding the transfer mode is essential for enhancing process control and the quality of the depositions. To develop a comprehensive understanding of the characteristics of the μ-GMA transfer mode, high-speed

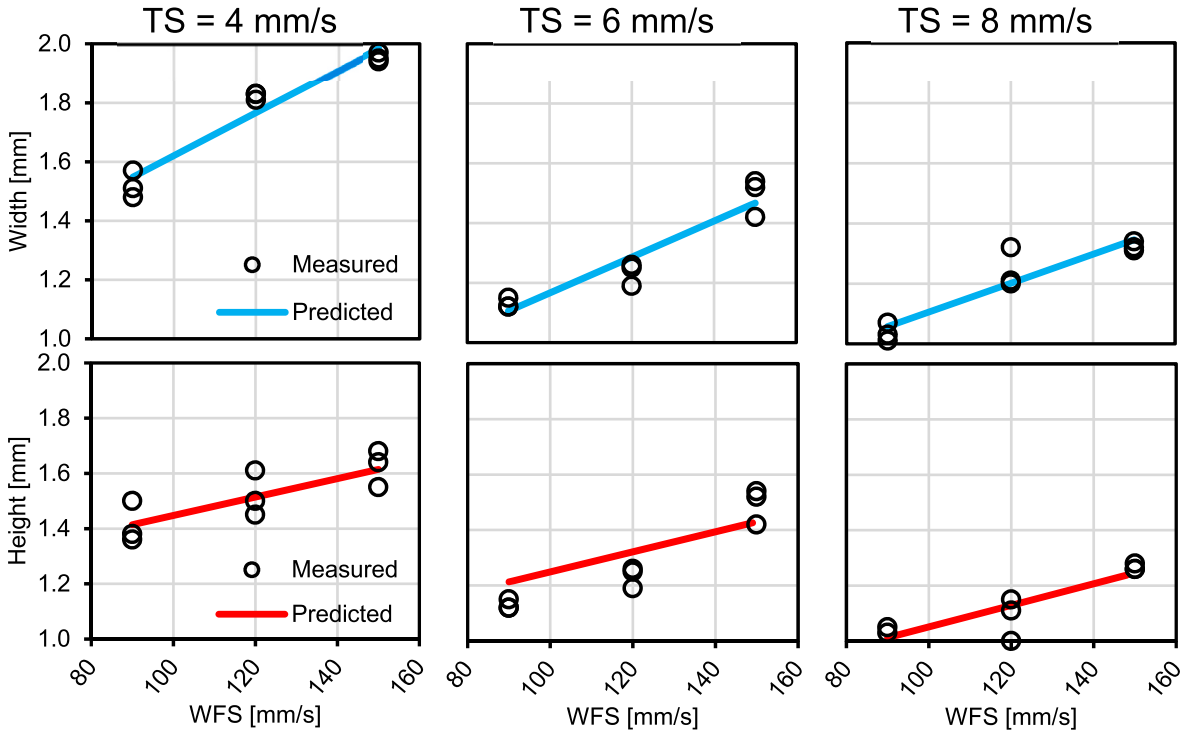

Fig. 9. Individual effects of TS and WFS on bead width and height.

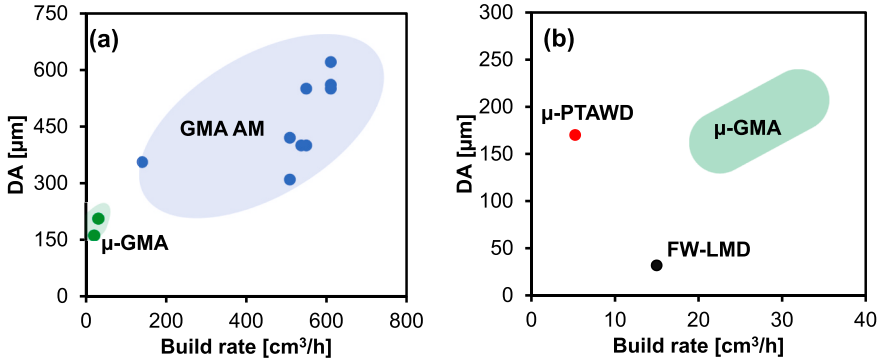

Fig. 10. Comparision between μ-GMA with (a) GMA-based DED [28,43,44], and (b) μ-DED [17,27,45] technologies by terms of dimensional accuracy (DA) and build rate.

imaging was utilized during a single-bead deposition. Fig. 8 displays frames from the high-speed recording of the deposition, along with the corresponding voltage and current curves during the metal transfer. The numbers corresponding to each frame are indicated in Fig. 8b, c, and 8d as I–V curves.

Initially, the first frame (1) shows an open circuit, where the wire does not touch the deposited layer. The curvature observed in the 'molten pool' images suggests that the viscosity of the molten metal is higher than in typical GMA welding. Therefore, it is reasonable to consider that this region is a lower temperature zone or even a mushy zone. The low heat input and consequently high cooling rate of this deposition corroborate this assumption. In the second frame (2), the electrode tip touches the substrate, initiating a short-circuit, identified by a sharp increase in the current flow. Notice a ~0.1 ms plateau of current and voltage, which could indicate a quick establishment of an electric arc, although it was not possible to clearly identify this during the high-speed recording. Frames 3 and 4 show that the electrode's extension (stick-out) begins to heat due to the Joule effect. Note that there is a slight decrease in the current plateau during this period, which can be explained by the increase in the wire's resistivity as its temperature rises. From this point onward, this transfer mechanism is similar to the conventional short-circuit transfer mode. The current flow produces a magnetic field that applies an inductive force. This inductance acts as a pinch force, proportional to the square of the current [35]. Thus, when the current reaches high values, the pinch force squeezes the metal droplet from the tip of the wire electrode (frame 5) until it narrows enough to break the short circuit (frames 6 and 7). After the transfer of the metal droplet, the current still flows through a short-period electric arc (frame 6) until it ends in an open circuit (frame 8).

The V–I curve suggests ignition and reignition of an electric arc in frames 2 and 6, respectively. In both cases, when the distance (d) between the electrodes approaches 0 mm, i.e., just before the opening of the short-circuit and immediately after the droplet transfer, the electrode tip undergoes significant heating. It is reasonable to assume that energetic electrons are emitted from the surface of the electrode tip through thermionic emission. Due to the voltage applied by the power

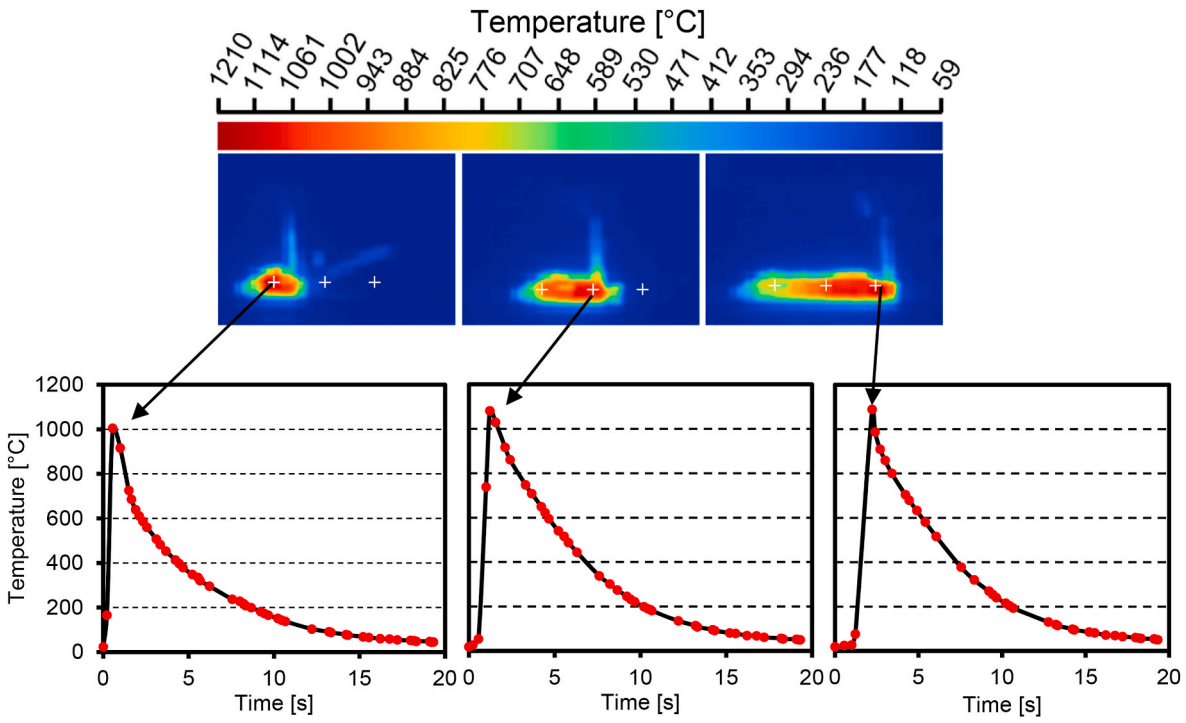

Fig. 11. Thermographic analysis of the μ-GMA deposition illustrating the temperature profile measures.

Table 5
Temperature data extracted from thermography measurements of the μ-GMA single-bead depositions, and a regular GMA-based DED deposition [20].

Ø Wire [mm]	Bead	WFS [mm/s]	TS [mm/s]	H [J/mm]	$t_{800-500}$ [s]	Cooling rate [°C/s]
0.3	1	120	5	81.7	2.64	113.6
	2				4.56	65.8
1[a]	1	50	3.9	511	47.1	6.37

[a] Values extracted from Ref. [28].

Table 6
μ-GMA and GMA-based DED bead dimensions, and calculated perimeter/area ratio [20].

Ø Wire [mm]	Heat input [J/mm]	Width [mm]	Height [mm]	Area [mm^2]	Perimeter [mm]	Perimeter/Area [mm^{-1}]
0.30	81.7	1.10 ± 0.1	0.88 ± 0.1	0.69[c]	3.15[c]	4.58
1[a]	511.0	8.80 ± 0.6	1.30 ± 0.1	8.98[b]	15.87[b]	1.77

[a] Values extracted from Ref. [28].
[b] Theoretical values calculated considering the width and height as the semi-axes of an ellipse.
[c] The measurements were obtained from a cross-sectional micrograph using ImageJ software.

supply, these electrons are accelerated towards the anode, resulting in a flow of current. This mechanism reduces the breakdown voltage (as d → 0) to smaller values, facilitating arc ignition.

The extinction of the electric arc after the droplet transfer (frame 6) can be attributed to a combination of factors. Studies have described arc characteristics based on electrode distance and shielding gas (e.g., Ar, He) [36,37]. The term 'operational points' refers to the intersections between the power source and arc characteristic curves, which occur at two points. GMA-based DED depositions operate at the higher current point, representing a stable region on the arc characteristic curve. However, due to the necessity of using a smaller current for a micrometric wire, the operational point of the μ-GMA deposition falls within the unstable region of the arc characteristics. Minor fluctuations in both voltage and current around this operational point can potentially lead to the extinguishing of the electric arc. Therefore, during droplet transfer, the extinction of the short-circuit is accompanied by an explosion of the bridge wire-molten pool. This behavior applies a force in the opposite direction of the feeding, causing the electrode to move away and increasing the length of the arc (from frame 6 to 7). Subsequently, due to its inherent characteristics, the arc becomes unstable and is extinguished (frame 8). As the wire feed continues, the cycle repeats (frame 1). The poor appearance of the surface wall shown in Fig. 6 is justified by the unstable mechanism of the transfer mode. However, the wall DA value obtained is superior to that of GMA-based DED depositions (see section 3.5). Further work will be undertaken to optimize this issue.

Notice in Fig. 8b that the frequency of the μ-GMA short-circuit transfer was about 5 kHz, significantly higher than the 20–200 Hz frequency of short-circuit depositions in GMA-based DED (Ø 1–1.2 mm) [38]. Several distinct phenomena occurred as previously described, rendering the transfer modes conventionally recognized in GMA-based DED not directly applicable in this context. Therefore, it should be concluded that the dynamics of metallic transfer are markedly distinct in both cases, signifying that μ-GMA cannot be merely denominated as a scaling factor of GMA-based AM.

3.2. Influence of WFS and TS on bead dimensions

WFS and TS are the key operational parameters in GMA-based DED processes. It is well-known that control of WFS and TS is fundamental to ensuring good quality of the deposited beads (i.e., width and height). In order to develop a comprehensive understanding of the influence of these parameters on μ-GMA single-bead depositions, a 2^2 factorial design of experiment (DOE) was performed within the previously determined work window (Fig. 5). The effects of TS and WFS on the BW and BH of single-bead depositions were investigated. The parameters under this study were evaluated at both low and high levels, each with 3

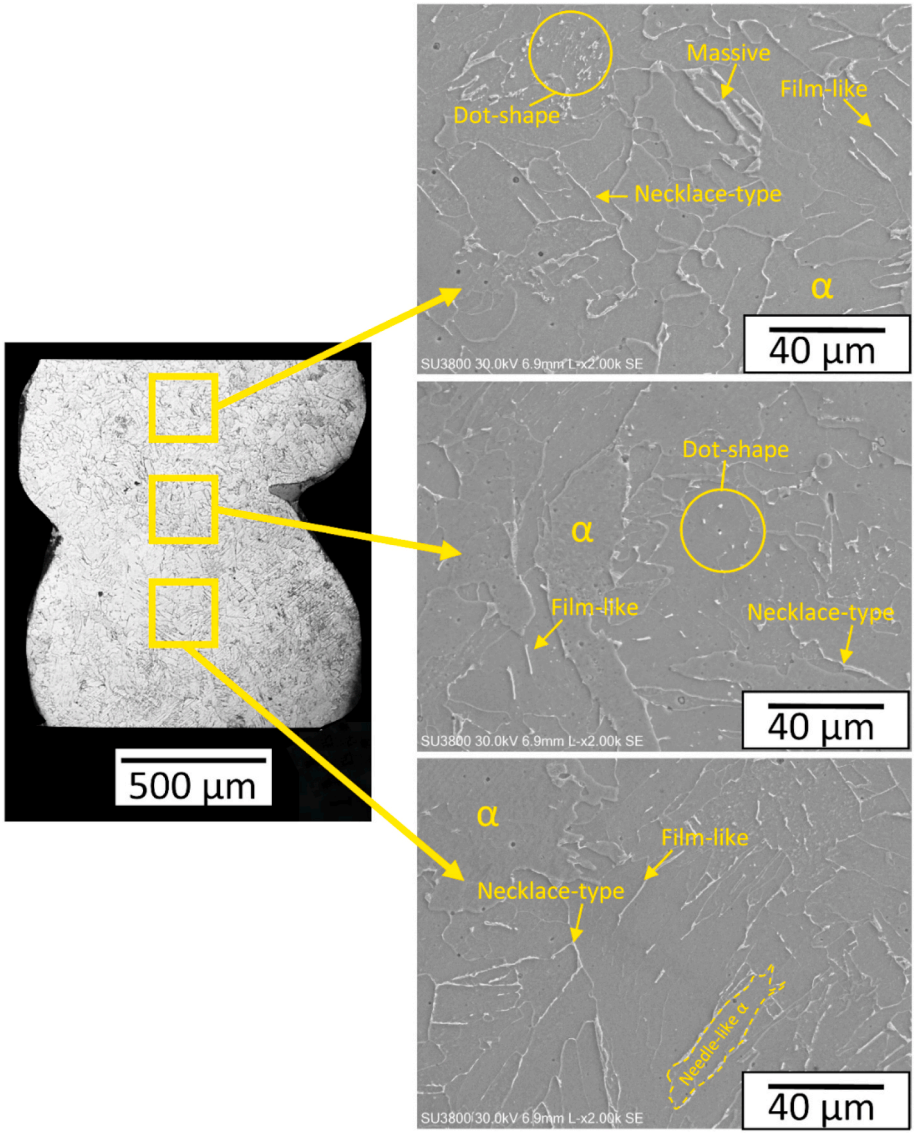

Fig. 12. Optical (left) and scanning electron (right) micrographs of a μ-GMA deposited 2-bead wall.

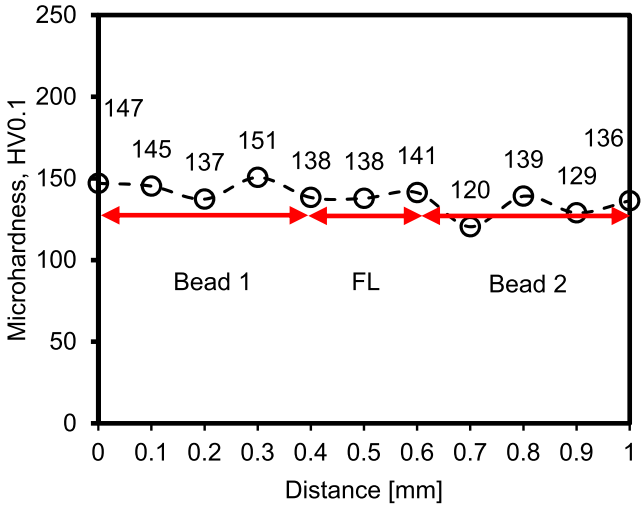

Fig. 13. Microhardness profile performed in the 2-bead wall from a μ-GMA deposition. FL stands for fusion line.

replicates. Additionally, a central point was introduced to examine the interaction effects between WFS and TS, resulting in a total of 27 randomized runs. To enhance the degree of error freedom and consequently improve the accuracy of the statistical analysis, non-significant second-order interactions were disregarded. Table 3 presents a summary of the process parameters employed in the DOE. The test plan, the randomized order of depositions, the corresponding values of WFS and TS, and the measurements of BW and BH are available in the supplementary material file.

By employing response surface methodology (RSM) integrated with Minitab v21 software, non-linear regression equations were established to correlate BW (equation IV) and BH (equation V) with the investigated μ-GMA deposition parameters. Table 4 shows good fitness of the regression statistics obtained from equations IV and V. The adjusted and predicted R^2 (R^2_{adj} and R^2_{pred} terms, respectively) values for all models remain consistent with the original R^2 value, suggesting that simplified models adequately describe the data without incorporating unnecessary model terms. This indicates that equations IV and V effectively capture the data without the risk of overfitting caused by an excessive number of model terms.

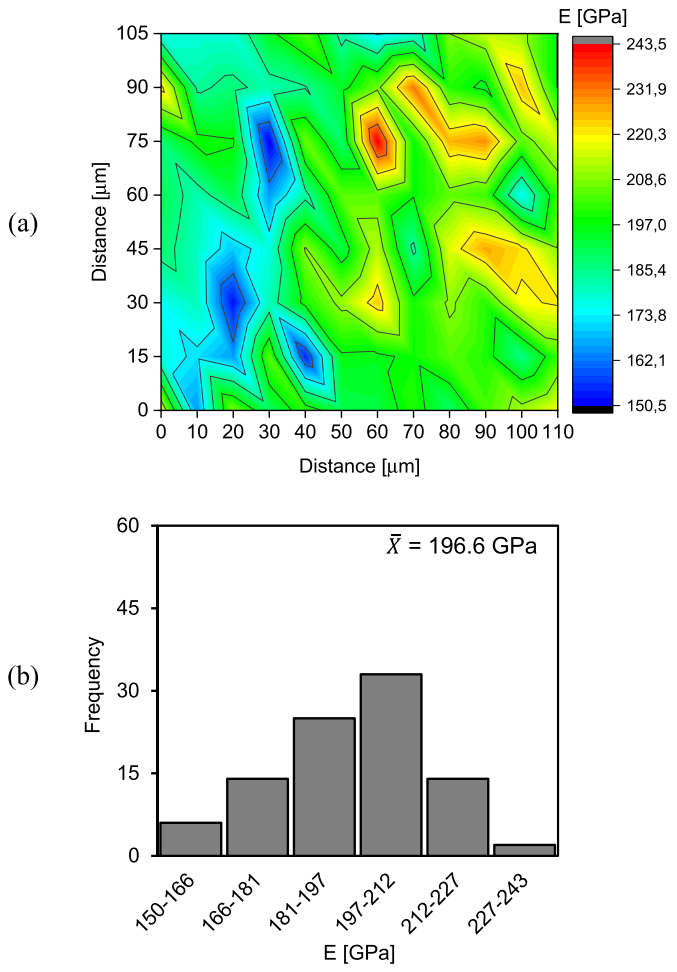

Fig. 14. (A) Reduced Young's modulus map performed at the center of the first bead of the µ-GMA sample, and the (b) frequency distribution of the measurements.

$$BW = 2.750 - 6.61 \bullet 10^{-1} \bullet TS + 4.95 \bullet 10^{-2} \bullet TS^2 + 9.69 \bullet 10^{-3} \bullet WFS + 6.11 \bullet 10^{-4} \bullet WFS \bullet TS \quad (4)$$

$$BH = 1.574 - 1.15 \bullet 10^{-1} \bullet TS + 2.78 \bullet 10^{-3} \bullet WFS + 1.39 \times 10^{-4} \bullet WFS \bullet TS \quad (5)$$

The adequacy and acceptability of the derived regression equations IV and V were assessed by conducting ANOVA tests using Minitab v21 software, with a confidence level of 95%. ANOVA statistical analysis of BW and BH, including the effects of WFS, TS, TS^2, and the interaction term WFS × TS, was performed. The squared interaction effect WFS^2 was excluded for BW, and all squared interaction terms for BH were excluded due to their lack of significant contribution to the response variable. ANOVA statistical analyses of BW and BH are available in the supplementary material file. Additionally, the effectiveness of the ANOVA analyses was demonstrated by the residual plots, which are also available in the supplementary material. In these plots, the residuals adhere to a normal distribution, and the residuals versus fit values plot shows that the assumption of constant variance was satisfied.

The ANOVA analysis reveals the significance of WFS and TS as factors impacting BW and BH. Among these, TS emerges as the primary influential factor, followed by WFS, and subsequently the interaction effect of WFS × TS, which exhibits marginal significance. Equations IV and V underscore the contrasting effects of TS and WFS on bead dimensions. The dimensions of the bead are contingent on the volume of molten metal deposition. Therefore, the increase in TS and WFS leads to a thinning and thickening effect on bead width and height, respectively. However, as the ANOVA analysis demonstrated, the influence of TS outweighs that of WFS within the explored value ranges. The discrete effects of TS and WFS on BW and BH are visualized in Fig. 9.

Thus, despite the differences in metallic transfer mode, the impact of TS and WFS on bead dimensions in µ-GMA depositions corresponds with findings from previous GMA studies [39–42]. However, in the case of the µ-GMA process, TS demonstrates primary influence on both BH and BW within the range of studied deposition parameters.

3.3. Dimensional accuracy

Dimensional accuracy (DA) is typically used to gauge the alignment between design specifications and the actual dimensions of

Table 7
Comparison between µ-GMA and a GMA-based DED processes by terms of process characteristics. GMA-based DED data was extracted from Ref. [28].

	Unit	GMA-based DED*	µ-GMA	GMA-based DED/ µ-GMA
Wire diameter	[mm]	1.0	0.3	3.3
Wire feeding speed	[mm/s]	50.0	120.0	0.4
Travel speed	[mm/s]	3.9	6.0	0.7
Power	[W]	1995.0	408.70	4.9
Heat input	[J/mm]	511.5	82.0	6.2
Cooling rate $_{1st\ bead}$	[°C/s]	6.37	121.52	0.05
Energy density	[J/mm^3]	50.8	48.2	1.1
Bead thickness	[mm]	5.50 ± 0.6	1.10 ± 0.1	5.0
Dimensional accuracy	[µm]	356 ± 16	184 ± 22	1.9
Build rate	[cm^3/h]	141.4	30.5	4.6

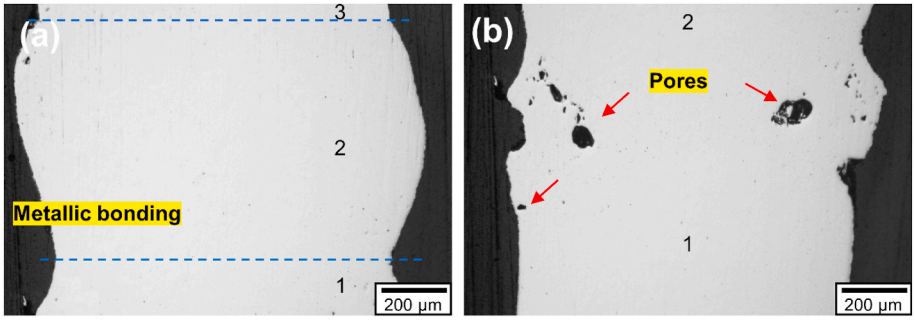

Fig. 15. Cross-sectional micrography showing (a) metallic bonding among the beads, and (b) defects such as pores resulting due to gas entrapment.

manufactured parts. DA was calculated as the average value from three cross-sectional cuts of a μ-GMA wall deposited using WFS = 120 mm/s and TS = 5 mm/s (Fig. 6). The obtained average value was SW = 184 ± 22 μm for a build rate of 30.5 cm^3/h. Fig. 10 contrasts the obtained DA values of μ-GMA with data extracted from literature for GMA-based AM and μ-DED processes (PTAWD and FW-LMD). It is well-known that there is a trade-off between DA and build rate. Fig. 10a demonstrates that μ-GMA can deposit thinner beads with smoother DA compared to regular GMA-based DED depositions. Additionally, μ-GMA has a higher build rate and yields DA close to some μ-DED processes, as illustrated in Fig. 10b. However, it is important to emphasize that at this time, this work does not propose that the μ-GMA prototype competes with μ-DED processes at any level; this comparison only aims to showcase its capability and potential. Future work will focus on optimizing this trade-off between DA and build rate.

3.4. μ-GMA cooling rate characteristcs

The cooling time between 800 and 500 °C ($t_{8/5}$) is a critical process indicator as it governs the main phase transformations in high-strength low-alloy steels [46,47]. Since the cooling rate is determined by the temperature gradient between the molten metal and its surroundings, $t_{8/5}$ is influenced by factors such as heat input (H), preheating, and interpass temperatures. Consequently, precise control of H is essential for managing the solidification microstructure and mechanical properties of the deposited beads. The observed H values in μ-GMA deposition are relatively lower (around 80 J/mm) compared to regular GMA-based DED (ranging from 200 to 500 J/mm [28]). To assess the influence of H on $t_{8/5}$, thermographic analysis was conducted during the 2-bead deposition with H = 82 J/mm. Three temperature profiles were extracted from the first and second beads, representing the beginning, middle, and end of each bead, as shown in Fig. 11. The cooling rate was calculated as the average among these three temperature profiles between 800 and 500 °C. The results are presented in Table 5.

Notice that the cooling rate of μ-GMA depositions is considerably higher than regular GMA-based DED deposition. This behavior occurs mainly due to two reasons: i) the lower heat input promotes a higher temperature gradient between the wire/mushy zone and the environment, increasing the cooling rate, and ii) the proportion of surface area to volume of μ-GMA deposited bead is higher, and consequently, it exchanges more heat by convection and radiation, accelerating the cooling rate. Table 6 shows the dimensions of μ-GMA and GMA-based DED beads, along with the calculated perimeter/area ratio.

3.5. Microstructural analysis

Fig. 12 shows an optical micrograph of the 2-bead wall (left side) and SEM micrographs of the first bead, fusion line, and second bead (right side). The sample matrix consisted entirely of ferrite (α), exhibiting various morphologies of martensite-austenite constituents (M-A). These included dot-shaped M-A dispersed within the α matrix, film-like M-A occurring within α grains, necklace-type M-A characterized by occurrences along the boundaries of α grains, and massive M-A. The latter was distinguished by a core-shell structure, where martensite forms the outer region (shell), and austenite constitutes the inner region (core) [48]. The formation of M-A constituents is linked to the high cooling rates of μ-GMA deposition. During solidification, the austenite γ tends to transform into ferrite α, undergoing a change in its crystalline structure from face-centered cubic (FCC) to body-centered cubic (BCC), a structure with higher atomic packing efficiency. However, this transformation requires both temperature and time for the diffusion of solubilized alloying elements, which is limited due to the rapid cooling rates of μ-GMA. Consequently, a metastable phase forms, known as M-A. The formation of massive M-A constituents in the second bead is also notable. The cooling rate of the overlap bead is reduced owing to the interpass temperature, resulting in a smaller thermal gradient. The occurrence of massive M-A formations over film-like M-A due to the decreased cooling rate is well-documented in the literature [48–52].

3.6. Vickers microhardness and reduced Young's modulus

Fig. 13 shows a Vickers microhardness profile measured from the center of the first bead to the center of the second one. There was no significant variation in microhardness across the wall cross-section, as anticipated due to the fully ferritic matrix observed. Despite the high cooling rates, the low microhardness values are attributed to the soft characteristics of the ferritic matrix in low-carbon steels [53].

The nanoindentation test is frequently employed for assessing local mechanical properties, enabling the measurement of the elastic modulus (NE) at a micrometer or nanometer scale. Due to the challenges of machining tensile test samples from μ-GMA depositions, nanoindentation measures allow us to evaluate these properties effectively. In this context, a nanoindentation map was performed at the center of the first bead, as shown in Fig. 14a. Fig. 14b displays the frequency distribution of NE across the test sample.

The NE map showed an average value of 196 GPa. Tankova et al. [54], Ermakova et al. [55], and Langui et al. [56] reported Young's modulus (E) values in the range of 181–221 GPa for low-carbon steel parts produced by GMA-based DED. Therefore, despite the unique characteristics of μ-GMA, such as a faster cooling rate and intermittent short-circuit transfer mode, these preliminary results indicate that μ-GMA can deposit low-carbon steel walls with mechanical properties comparable to those of regular GMA-based DED depositions. However, further work will be conducted to evaluate other important mechanical properties, such as impact toughness.

4. Limitations of the current prototype

The μ-GMA prototype has demonstrated its capability to deposit a wall with metallic bonding between the beads, as illustrated in Figs. 12 and 15a. However, the applied currents during deposition typically range from 30% to 40% of those used in low-current GMA-based DED processes, which can result in deposition issues such as lack of fusion. Due to its high cooling rate, typical defects may occur, including inclusions, high residual stress, and hydrogen cracking. Moreover, solidification defects can be exacerbated by gas entrapment, leading to the formation of cracks and pores, as depicted in Fig. 15b. During solidification, hydrogen atoms are expelled from the solid phase and migrate to the liquid phase across the liquid/solid interface (due to differences in hydrogen solubility between them [57]), thereby increasing the hydrogen content in the liquid phase. If the concentration of hydrogen atoms in the liquid steel exceeds the solubility limit, bubble formation initiates. Owing to the rapid cooling rate of μ-GMA, the molten pool solidifies swiftly, hindering the diffusion of some bubbles to the surface and their release into the atmosphere. Consequently, the solidified metal entraps the migrating bubbles near the surface, leading to pore formation [58,59] (as indicated in Fig. 15b). Additionally, the formation of brittle microstructures/phases depending on the chemical composition of the filler metal is also possible. For instance, high-C, high-strength low alloy, and ferritic stainless steels are susceptible to such effects. However, these defects can be mitigated by implementing solutions such as controlled preheating, adjustment of deposition parameters, adequate molten pool shielding, environmental humidity control, and post-heating for stress relief. It is important to emphasize that this is a pioneering prototype of an ongoing project, and future developments will aim to achieve even better results.

5. Summary and conclusions

Table 7 summarizes the main process characteristics of μ-GMA prototype in contrast to a regular GMA-based DED deposition.

This work proposed to develop a gas metal arc based direct energy

deposition prototype to deposit micrometric wires and assess its technical feasibility. The major conclusions are as follows.

- μ-GMA prototype demonstrated the capability to deposit beads with an approximate width of 1 mm, nearly 5 times thinner than standard GMA-based DED deposition. This result was achieved with a build rate of 30 cm^3/h, which is lower than GMA-based DED indeed, but higher than other μ-DED processes.
- The transfer mode characteristics of μ-GMA deposition are short-circuit-based with an intermittent electric arc, featuring a metallic transfer frequency of about 5 kHz, which is significantly higher than that of GMA-based DED depositions.
- Microstructural analyses revealed that the sample matrix was composed entirely of ferrite with martensite-austenite constituents. The microhardness showed no significant variation across the wall cross-section. Finally, the nanoindentation map indicates that μ-GMA can deposit low-carbon steel walls with mechanical properties comparable with regular GMA-based DED depositions.
- Statistical analysis demonstrated that both WFS and TS significantly impact the bead width and height of μ-GMA depositions. TS and WFS exhibit a direct thinning and thickening effect on bead width and height, respectively.

Therefore, the development of the μ-GMA prototype leveraged the advantages of GMA-based DED systems and employed a downscaling approach to enhance the resolution of the printed parts, closely approaching μ-DED in dimensional accuracy. Furthermore, the material availability of micrometric diameter drawn wires for this prototype is higher than for conventional GMA-based DED. In addition, the low heat input characteristics of μ-GMA deposition are attractive when working with heat-sensitive alloys such as austenitic stainless steel, aluminum alloys, and nickel and cobalt-based superalloys. Further work will be conducted to assess the deposition of a range of metals.

Funding

Authors acknowledge the Portuguese Fundação para a Ciência e a Tecnologia (FCT - MCTES) for its financial support via the project UID/EMS/00667/2019 (UNIDEMI). P. H. G. Dornelas acknowledges FCT - MCTES for funding the PhD grant 2021.05298.BD. JPO acknowledges funding by national funds from FCT - Fundação para a Ciência e a Tecnologia, I.P., in the scope of the projects LA/P/0037/2020, UIDP/50025/2020 and UIDB/50025/2020 of the Associate Laboratory Institute of Nanostructures, Nanomodelling and Nanofabrication – i3N. This activity has received funding from the European Institute of Innovation and Technology (EIT) RawMaterials through the project Smart WAAM: Microstructural Engineering and Integrated Non-Destructive Testing. This body of the European Union receives support from the European Union's Horizon 2020 research and innovation program. This research is sponsored by national funds through FCT - Fundação para a Ciência e a Tecnologia , under projects UIDB/00285/2020 and LA/P/0112/2020

CRediT authorship contribution statement

Paulo Henrique Grossi Dornelas: Formal analysis, Investigation, Method, Writing – original draft, Writing – review & editing. **J.P. Oliveira:** Formal analysis, Funding acquisition, Project administration, Supervision, Writing – review & editing. **Tadeu Castro da Silva:** Funding acquisition, Writing – review & editing. **A.S. Ramos:** Funding acquisition, Writing – review & editing. **Telmo G. Santos:** Formal analysis, Funding acquisition, Project administration, Supervision, Writing – review & editing.

Declaration of competing interest

The authors declare that they have no known competing financial interests or personal relationships that could have appeared to influence the work reported in this paper.

Appendix A. Supplementary data

Supplementary data to this article can be found online at https://doi.org/10.1016/j.jmrt.2024.04.056.

References

[1] Shukla M, Todorov I, Kapletia D. Application of additive manufacturing for mass customisation: understanding the interaction of critical barriers. Prod Plann Control 2018;29:814–25. https://doi.org/10.1080/09537287.2018.1474395.
[2] Thomas DS, Gilbert SW. Costs and cost effectiveness of additive manufacturing. Gaithersburg, MD. 2014. https://doi.org/10.6028/NIST.SP.1176.
[3] Sepasgozar SME, Shi A, Yang L, Shirowzhan S, Edwards DJ. Additive manufacturing applications for Industry 4.0: a systematic critical review. Buildings 2020;10:231. https://doi.org/10.3390/buildings10120231.
[4] Chua CK, Chou SM, Wong TS. A study of the state-of-the-art rapid prototyping technologies. Int J Adv Des Manuf Technol 1998;14:146–52. https://doi.org/10.1007/BF01322222.
[5] Gurr M, Mülhaupt R. Rapid prototyping. Reference module in materials science and materials engineering. Elsevier; 2016. https://doi.org/10.1016/B978-0-12-803581-8.01477-6.
[6] Lee H, Lim CHJ, Low MJ, Tham N, Murukeshan VM, Kim Y-J. Lasers in additive manufacturing: a review. International Journal of Precision Engineering and Manufacturing-Green Technology 2017;4:307–22. https://doi.org/10.1007/s40684-017-0037-7.
[7] Dev Singh D, Mahender T, Raji Reddy A. Powder bed fusion process: a brief review. Mater Today Proc 2021;46:350–5. https://doi.org/10.1016/j.matpr.2020.08.415.
[8] Svetlizky D, Das M, Zheng B, Vyatskikh AL, Bose S, Bandyopadhyay A, et al. Directed energy deposition (DED) additive manufacturing: physical characteristics, defects, challenges and applications. Mater Today 2021;49:271–95. https://doi.org/10.1016/j.mattod.2021.03.020.
[9] Cipriano Farias FW, Rebelo Duarte V, da Cruz Payão Filho J, Schell N, Maawad E, Bordas-Czaplicki M, et al. Arc-based directed energy deposited Inconel 718: role of heat treatments on high-temperature tensile behavior. Mater Res Lett 2024;12:97–107. https://doi.org/10.1080/21663831.2023.2297734.
[10] Farias FWC, dos Santos TJG, Oliveira JP. Directed energy deposition + mechanical interlayer deformation additive manufacturing: a state-of-the-art literature review. Int J Adv Des Manuf Technol 2024. https://doi.org/10.1007/s00170-024-13126-5.
[11] Dornelas PHG, Santos TG, Oliveira JP. Micro-metal additive manufacturing – state-of-art and perspectives. Int J Adv Des Manuf Technol 2022;122:3547–64. https://doi.org/10.1007/s00170-022-10110-9.
[12] Horii T, Kirihara S, Miyamoto Y. Freeform fabrication of Ti–Al alloys by 3D micro-welding. Intermetallics 2008;16:1245–9. https://doi.org/10.1016/j.intermet.2008.07.009.
[13] Horii T, Kirihara S, Miyamoto Y. Freeform fabrication of superalloy objects by 3D micro welding. Mater Des 2009;30:1093–7. https://doi.org/10.1016/j.matdes.2008.06.033.
[14] Terakubo M, Oh J, Kirihara S, Miyamoto Y, Matsuura K, Kudoh M. Freeform fabrication of Ti–Ni and Ti–Fe intermetallic alloys by 3D Micro Welding. Intermetallics 2007;15:133–8. https://doi.org/10.1016/j.intermet.2006.03.012.
[15] Katou M, Oh J, Miyamoto Y, Matsuura K, Kudoh M. Freeform fabrication of titanium metal and intermetallic alloys by three-dimensional micro welding. Mater Des 2007;28:2093–8. https://doi.org/10.1016/j.matdes.2006.05.024.
[16] Terakubo M, Oh J, Kirihara S, Miyamoto Y, Matsuura K, Kudoh M. Freeform fabrication of titanium metal by 3D micro welding. Mater Sci Eng, A 2005;402:84–91. https://doi.org/10.1016/j.msea.2005.04.025.
[17] Jhavar S, Jain NK, Paul CP. Development of micro-plasma transferred arc (μ-PTA) wire deposition process for additive layer manufacturing applications. J Mater Process Technol 2014;214:1102–10. https://doi.org/10.1016/j.jmatprotec.2013.12.016.
[18] Jhavar S, Paul CP, Jain NK. Micro-plasma transferred arc additive manufacturing for die and mold surface remanufacturing. JOM 2016;68:1801–9. https://doi.org/10.1007/s11837-016-1932-z.
[19] Sawant MS, Jain NK. Characteristics of single-track and multi-track depositions of stellite by micro-plasma transferred arc powder deposition process. J Mater Eng Perform 2017;26:4029–39. https://doi.org/10.1007/s11665-017-2828-y.
[20] Jain N, Sawant M, Nikam S, Jhavar S. Metal deposition: plasma-based processes. Encyclopedia of Plasma Technology, CRC Press; 2016. p. 722–40. https://doi.org/10.1081/E-EPLT-120053919.
[21] Sawant MS, Jain NK. Investigations on wear characteristics of Stellite coating by micro-plasma transferred arc powder deposition process. Wear 2017;378–379:155–64. https://doi.org/10.1016/j.wear.2017.02.041.
[22] Kim S-Y, Park G-H, Kim H-A, Lee A-Y, Oh H-R, Lee C-W, et al. Micro-deposition of Cu-based metallic glass wire by direct laser melting process. Mater Lett 2017;202:1–4. https://doi.org/10.1016/j.matlet.2017.05.092.
[23] Demir AG. Micro laser metal wire deposition for additive manufacturing of thin-walled structures. Opt Lasers Eng 2018;100:9–17. https://doi.org/10.1016/j.optlaseng.2017.07.003.

[24] Demir AG, Biffi CA. Micro laser metal wire deposition of thin-walled Al alloy components: process and material characterization. J Manuf Process 2019;37:362–9. https://doi.org/10.1016/j.jmapro.2018.11.017.
[25] Gökhan Demir A. Single track deposition study of biodegradable Mg-rare earth alloy by micro laser metal wire deposition. Mater Today Proc 2019;7:426–34. https://doi.org/10.1016/j.matpr.2018.11.105.
[26] Biffi CA, Tuissi A, Demir AG. Martensitic transformation, microstructure and functional behavior of thin-walled Nitinol produced by micro laser metal wire deposition. J Mater Res Technol 2021;12:2205–15. https://doi.org/10.1016/j.jmrt.2021.03.108.
[27] Shaikh MO, Chen C-C, Chiang H-C, Chen J-R, Chou Y-C, Kuo T-Y, et al. Additive manufacturing using fine wire-based laser metal deposition. Rapid Prototyp J 2019;26:473–83. https://doi.org/10.1108/RPJ-04-2019-0110.
[28] Rodrigues TA, Duarte V, Avila JA, Santos TG, Miranda RM, Oliveira JP. Wire and arc additive manufacturing of HSLA steel: effect of thermal cycles on microstructure and mechanical properties. Addit Manuf 2019;27:440–50. https://doi.org/10.1016/j.addma.2019.03.029.
[29] Kumar V, Ranjan Sahu D, Mandal A. Parametric study and optimization of GMAW based AM process for Multi-layer bead deposition. Mater Today Proc 2022;62:255–61. https://doi.org/10.1016/j.matpr.2022.03.223.
[30] Rosli A, Alkagari M, Ramli F, Abdollah M. Influence of process parameter on the height deviation of weld bead in wire arc additive manufacturing. Int J Mech Prod Eng Res Dev 2020;10:1165–76.
[31] Yang D, Wang G, Zhang G. Thermal analysis for single-pass multi-layer GMAW based additive manufacturing using infrared thermography. J Mater Process Technol 2017;244:215–24. https://doi.org/10.1016/j.jmatprotec.2017.01.024.
[32] Martina F, Mehnen J, Williams SW, Colegrove P, Wang F. Investigation of the benefits of plasma deposition for the additive layer manufacture of Ti–6Al–4V. J Mater Process Technol 2012;212:1377–86. https://doi.org/10.1016/j.jmatprotec.2012.02.002.
[33] Oliver WC, Pharr GM. An improved technique for determining hardness and elastic modulus using load and displacement sensing indentation experiments. J Mater Res 1992;7:1564–83. https://doi.org/10.1557/JMR.1992.1564.
[34] American Welding Society. Welding processes, vol. 2. RL O'Brien; 1991.
[35] Kah P, Latifi H, Suoranta R, Martikainen J, Pirinen M. Usability of arc types in industrial welding. Int J Mech Mater Eng 2014;9:15. https://doi.org/10.1186/s40712-014-0015-6.
[36] Sawicki A. An integral method for determining the parameters of the universal electric arc model describing an arc with a hyperboliclinear static characteristic. Przeglad Elektrotechniczny 2016;1:164–7. https://doi.org/10.15199/48.2016.07.35.
[37] Andrea J, Schweitzer P, Carvou E. Comparison of equations of the VI characteristics of an electric arc in open air. 2019 IEEE holm conference on electrical contacts. IEEE; 2019. p. 76–81. https://doi.org/10.1109/HOLM.2019.8923912.
[38] Singh R. Welding and joining processes. Applied welding engineering. Elsevier; 2020. p. 157–86. https://doi.org/10.1016/B978-0-12-821348-3.00015-X.
[39] Xiong J, Li Y, Li R, Yin Z. Influences of process parameters on surface roughness of multi-layer single-pass thin-walled parts in GMAW-based additive manufacturing. J Mater Process Technol 2018;252:128–36. https://doi.org/10.1016/j.jmatprotec.2017.09.020.
[40] Chandrasekaran RR, Benoit MJ, Barrett JM, Gerlich AP. Multi-variable statistical models for predicting bead geometry in gas metal arc welding. Int J Adv Des Manuf Technol 2019;105:1573–84. https://doi.org/10.1007/s00170-019-04355-0.
[41] Chaudhari R, Parmar H, Vora J, Patel VK. Parametric study and investigations of bead geometries of GMAW-based wire–arc additive manufacturing of 316L stainless steels. Metals 2022;12:1232. https://doi.org/10.3390/met12071232.
[42] Le VT, Mai DS, Doan TK, Paris H. Wire and arc additive manufacturing of 308L stainless steel components: optimization of processing parameters and material properties. Engineering Science and Technology, an International Journal 2021;24:1015–26. https://doi.org/10.1016/j.jestch.2021.01.009.
[43] da Silva LJ, Teixeira FR, Araújo DB, Reis RP, Scotti A. Work envelope expansion and parametric optimization in WAAM with relative density and surface aspect as quality constraints: the case of Al5Mg thin walls with active cooling. Journal of Manufacturing and Materials Processing 2021;5:40. https://doi.org/10.3390/jmmp5020040.
[44] Scotti FM, Teixeira FR, Silva LJ da, de Araújo DB, Reis RP, Scotti A. Thermal management in WAAM through the CMT Advanced process and an active cooling technique. J Manuf Process 2020;57:23–35. https://doi.org/10.1016/j.jmapro.2020.06.007.
[45] Jhavar S, Jain NK, Paul CP. Enhancement of deposition quality in micro-plasma transferred arc deposition process. Mater Manuf Process 2014;29:1017–23. https://doi.org/10.1080/10426914.2014.892984.
[46] Dornelas PHG, Payão Filho J da C, Farias FWC, Moraes e Oliveira VHP, Moraes D de O, Zumpano Júnior P. FEM-thermodynamic simulation methodology to predict the influence of t8/5 on the coarse grain heat-affected zone of a Cr-Mo low-alloy steel pipe. J Manuf Process 2020;60:520–9. https://doi.org/10.1016/j.jmapro.2020.10.082.
[47] Dornelas PHG, Payão Filho J da C, Moraes e, Oliveira VHP, Moraes D de O, Zumpano Júnior P. Effect of the interpass temperature on simulated heat-affected zone of gas metal arc welded API 5L X70 pipe joint. Int J Adv Des Manuf Technol 2022;119:261–74. https://doi.org/10.1007/s00170-021-08261-2.
[48] Dornelas PHG, Payão Filho J da C, Moraes e, Oliveira VHP, Moraes D de O, Zumpano Júnior P. Influence of interpass temperature on the simulated HAZ of a clad API 5L X65 pipe joint welded with a gas metal arc. Weld World 2022;66:213–26. https://doi.org/10.1007/s40194-021-01244-7.
[49] Huda N, Midawi ARH, Gianetto J, Lazor R, Gerlich AP. Influence of martensite-austenite (MA) on impact toughness of X80 line pipe steels. Mater Sci Eng, A 2016;662:481–91. https://doi.org/10.1016/j.msea.2016.03.095.
[50] Luo X, Chen X, Wang T, Pan S, Wang Z. Effect of morphologies of martensite–austenite constituents on impact toughness in intercritically reheated coarse-grained heat-affected zone of HSLA steel. Mater Sci Eng, A 2018;710:192–9. https://doi.org/10.1016/j.msea.2017.10.079.
[51] Wang XL, Wang ZQ, Dong LL, Shang CJ, Ma XP, Subramanian SV. New insights into the mechanism of cooling rate on the impact toughness of coarse grained heat affected zone from the aspect of variant selection. Mater Sci Eng, A 2017;704:448–58. https://doi.org/10.1016/j.msea.2017.07.095.
[52] Dornelas PHG, Payão Filho J da C, Moraes e, Oliveira VHP, Moraes D de O, Zumpano Júnior P. Studying the influence of the interpass temperature on the heat-affected zone of an API 5L X65 steel welded pipe joint through computational and physical simulations. Int J Pres Ves Pip 2021;194:104548. https://doi.org/10.1016/j.ijpvp.2021.104548.
[53] Dornelas PHG, Payão Filho J da C, Farias FWC, Moraes e, Oliveira VHP, Moraes D de O, Zumpano Júnior P. Influence of the interpass temperature on the microstructure and mechanical properties of the weld metal (AWS A5.18 ER70S-6) of a narrow gap welded API 5L X70 pipe joint. Int J Pres Ves Pip 2022;199:104690. https://doi.org/10.1016/j.ijpvp.2022.104690.
[54] Tankova T, Andrade D, Branco R, Zhu C, Rodrigues D, Simões da Silva L. Characterization of robotized CMT-WAAM carbon steel. J Constr Steel Res 2022;199:107624. https://doi.org/10.1016/j.jcsr.2022.107624.
[55] Ermakova A, Mehmanparast A, Ganguly S, Razavi N, Berto F. Investigation of mechanical and fracture properties of wire and arc additively manufactured low carbon steel components. Theor Appl Fract Mech 2020;109:102685. https://doi.org/10.1016/j.tafmec.2020.102685.
[56] Laghi V, Arrè L, Tonelli L, Di Egidio G, Ceschini L, Monzón I, et al. Mechanical and microstructural features of wire-and-arc additively manufactured carbon steel thick plates. Int J Adv Des Manuf Technol 2023;127:1391–405. https://doi.org/10.1007/s00170-023-11538-3.
[57] Boeira AP, Ferreira IL, Garcia A. Alloy composition and metal/mold heat transfer efficiency affecting inverse segregation and porosity of as-cast Al–Cu alloys. Mater Des 2009;30:2090–8. https://doi.org/10.1016/j.matdes.2008.08.032.
[58] da Silva CLM, Scotti A. The influence of double pulse on porosity formation in aluminum GMAW. J Mater Process Technol 2006;171:366–72. https://doi.org/10.1016/j.jmatprotec.2005.07.008.
[59] Fang Y, Wang L, Sun L, Lyu F, Zhang J, Zhan X. Influence of heat flow on the grain morphology and porosity of wire arc additive manufactured 2319 aluminum alloy. Met Mater Int 2023. https://doi.org/10.1007/s12540-023-01553-0.